Nanoscale

PAPER

Check for updates

Synthesis of titanium phosphide by thermal ALD based on a novel phosphorus precursor†

Raul Zazpe, [ID] *[a,b] Jaroslav Charvot,[c] Jhonatan Rodriguez-Pereira, [ID] [a,b]
Luděk Hromádko,[a,b] Michal Kurka, [ID] [a] Kaushik Baishya,[b] Hanna Sopha,[a,b]
Filip Bureš [ID] [c] and Jan M. Macak [ID] [a,b]

Herein, we present for the first time the synthesis of titanium phosphide (Ti_xP_y) by thermal ALD based on the use of in-house synthesized Tris(trimethyltin)phosphide (TMT_3P) combined with titanium tetrachloride ($TiCl_4$) as the P- and Ti-precursor, respectively. The deposition process demonstrated followed ALD principles and revealed an ALD window between 175 °C and 225 °C. The Ti_xP_y thin films grown on substrates of different nature were characterized by several techniques, showing granular surfaces and electrical resistivities of the order of hundreds of Ohms. The effects of different ALD parameters such as deposition temperature, dosing time of both precursors, and the type of substrate on the chemical composition were extensively assessed by X-ray photoelectron spectroscopy (XPS). Interestingly, the results yielded the deposition of P-rich titanium phosphide and showed that its chemical composition depends on the deposition temperature and the type of substrate. Based on XPS results, a tentative description of the Ti_xP_y growth as a function of the number of ALD cycles was provided.

Introduction

In the last few years, the interest attracted by transition metal phosphides (TMPs) in different research fields has increased significantly. The slight electronegativity difference between P ($X \approx 2.1$) and most transition metals ($X \approx 1.3$–2.5) implies a moderately strong P–M bond with a ionic/covalent nature, which brings about outstanding physicochemical properties including high chemical and thermal stability, electrical conductivity and mechanical hardness. Two main metal phosphide groups have been distinguished as a function of the composition: phosphorus-rich and metal-rich phosphides, the latter displaying high metallic electrical conductivity and remarkable catalytic properties.[1] Due to these properties along with their low-cost, low-toxicity and abundance, TMPs have gained significant attention and have been demonstrated as functional and efficient materials in a wide number of applications including energy storage (batteries and supercapacitors),[2–5]

sensing,[6] hydrogenation catalysis,[7] electrocatalysis[8–10] and photocatalysis.[11,12] Nowadays the advances experienced by the nanofabrication technologies allow the manufacturing of one-dimensional, two-dimensional or three-dimensional structures at the nanometer scale such as porous materials, hierarchical designs and high aspect ratio structures, which exhibit far superior chemical, physical, and electrical properties compared to their bulk counterparts. Thus, the aforementioned applications take the advantages and benefits of functional nanostructured materials for attaining superior performance. However, complex nanostructured geometries can be highly demanding in terms of achieving uniform and conformal (ultra)thin films of secondary materials. To date, Atomic Layer Deposition (ALD) is the only deposition technique that can fulfill the requirements of uniform and conformal deposition regardless of the geometry of the substrate.[13,14]

ALD is a well-established thin film deposition technique based on gas phase chemical precursors exposed separately to the surface of the substrate followed by a purging step. Accordingly, the precursors react alternatively with the active sites of the surface by self-limiting gas–surface (precursor–substrate) reactions resulting in a layer-by-layer growth, while during the purging step the excess precursor and reaction byproducts are removed from the chamber. The conformality and the unparalleled sub-nanometer thickness control lie in the self-limiting nature of the chemical surface reactions, caused by the limited number of active surface sites (available to react with the gas phase precursor), restricting the growth

[a]*Center of Materials and Nanotechnologies, Faculty of Chemical Technology, University of Pardubice, Nam. Cs. Legii 565, 530 02 Pardubice, Czech Republic. E-mail: raul.zazpe@upce.cz*
[b]*Central European Institute of Technology, Brno University of Technology, Purkynova 123, 612 00 Brno, Czech Republic*
[c]*Institute of Organic Chemistry and Technology, Faculty of Chemical Technology, University of Pardubice, Pardubice 532 10, Czech Republic*
†Electronic supplementary information (ESI) available. See DOI: https://doi.org/10.1039/d5nr00457h

process to one layer per cycle under ideal conditions. Thus, the ALD cycle is repeated until the desired sheet thickness is achieved.

These appealing features have attracted a great interest from both academy and industry, and have led to a noteworthy increase in the type and number of materials deposited by ALD, including oxides, sulfides, nitrides and metals. However, it has been observed that at the early stage, the ALD process can deviate from the ideal layer-by-layer growth exhibiting a delay in the thin film nucleation, generally illustrated by island growth mode and before a steady growth per cycle (GPC) is attained.[15] The nucleation delay can be related to thermochemistry and activation barriers of the reactions involved in the ALD process,[16] a lack/low density of suitable functional groups (essentially chemisorption sites) on the substrate surface,[15] a steric hindrance caused by ligands of the precursor blocking active sites,[17] or large differences in the surface energy between the substrate and the material to be deposited, as usually observed in ALD processes of high surface energy metals on lower surface energy substrates.[18]

Regarding P-based materials, ALD has been the deposition method of choice for the P doping of Al_2O_3 and p-type ZnO thin films using P_2O_5 and trimethylphosphite as P precursors, respectively.[19,20] However, in the last few years the main research interest has been devoted toward the design and development of ALD processes for the synthesis of different metal phosphates, as recently reviewed by L. Henderick et al. in a comprehensive work.[21] In particular, important efforts have been devoted to the search of suitable P precursors to replace those originally used like PCl_3 and P_2O_5, principally due to corrosive/toxic byproducts formed, high deposition temperature and/or its low vapor pressure. Accordingly, based on novel P precursors, mainly trimethyl phosphate (TMP) and derivatives, a large number of metal phosphates have been synthesized by thermal ALD, including Al,[22,23] Ti,[23,24] and Fe,[25] among others. Nevertheless, the methoxy functional groups ($-OCH_3$) of TMP exhibited a limited reactivity toward hydroxyl groups and organometallic compounds, which resulted in a poor growth rate. In order to enhance the reactivity of TMP, T. Dobbelaere et al. developed a plasma ALD approach for the synthesis of Al phosphate achieving a significantly higher growth rate.[26] Subsequently, such a plasma ALD strategy was also successfully applied for the synthesis of zinc,[27] iron,[28] titanium,[29] vanadium,[30] nickel[31] and cobalt[31] phosphates. The ALD of P-based materials has been used in the synthesis of several metal phosphorus oxynitrides, such as LiPON,[32] NaPON,[33] MgPON[34] and TiPON,[35] which have been mainly explored as solid-electrolytes and electrode coatings in the field of Li-ion batteries.

In contrast to metal phosphates, the deposition of transition metal phosphides by ALD is in its very early infancy and needs to be developed. Until now, only a few processes for the deposition of metal phosphides by ALD have been reported. Based on Ni phosphate deposited by plasma ALD, L. Henderick et al. reported the synthesis of crystalline Ni_2P upon post-annealing treatment under a H_2 atmosphere at

950 °C.[31] Regarding direct ALD synthesis, CoP and GaP thin films were deposited by combining phosphine (PH_3) as the P precursor with bis(N-t-butyl-N'-ethylpropanimidamidato)cobalt and trimethylgallium, respectively.[36,37] However, PH_3 is difficult to handle and it is rather unreactive, what limits its application to plasma ALD. In parallel, other P precursors used have been tertiarybutylphosphine ($tBuPH_2$) and tris(dimethylamino) phosphine [$P(NMe_2)_3$] for the deposition of InP[38] and GaP[39] thin films, yet at the expense of temperatures above 320 °C to promote the reaction. Typical P precursors used for the synthesis of metal phosphides in CVD, which could represent potential ALD precursors, including PCl_3 and derivatives (e.g., cyclohexylphosphine), demand harsh conditions to form metal phosphides, which are not viable for application in ALD.[40–42]

The search for a viable way towards deposition of metal phosphides by ALD starts with a suitable phosphorus ALD precursor, which is principally related to other pnictogenides, namely As and Sb. Tris(trialkylsilyl)As/Sb were reported as useful ALD precursors used for the synthesis of GaAs,[43] elemental Sb,[44–46] and metal antimonides such as GaSb, GeSb, and AlSb.[44,47] Structurally related Tris(trimethylsilyl)phosphide (TMS_3P) turned out to be a suitable P-precursor for the synthesis of Co_2P thin films.[48] The reactivity of phosphides might be further extended and compared to that of nitrogen, where analogous Tris(trimethylsilyl)amine (TMS_3N) and its derivatives were examined as Lewis bases.[49] The Lewis basicity of nitrogen atoms in $(R_3M)_3N$ increases in the order: M = Si < Ge < Sn (R = alkyl), which implies that TMT_3N (Tris(trimethyltin) amine) is more reactive than TMS_3N. This was confirmed by the preparation of InN quantum dots, where TMT_3N reacted with Me_2InCl affording InN nanocrystals at 200–350 °C.[50] In contrast, TMS_3N showed diminished reactivity yielding only a very limited amount of low-quality InN quantum dots.[51] Inspired by these findings, two P compounds, known TMS_3P and novel Tris(trimethyltin)phosphide (TMT_3P), were synthesized and examined as potential P-precursors in the deposition of titanium phosphide (Ti_xP_y) by thermal ALD.

Experimental section

Differential scanning calorimetry (DSC)

The thermal properties of target molecules were measured by differential scanning calorimetry (DSC) with a Mettler-Toledo STARe System DSC 2/700 equipped with an FRS 6 ceramic sensor and cooling system HUBER TC100-MT RC 23. DSC thermograms of the target compounds were measured in alumina crucibles with a small hole in the lid under a N_2 inert atmosphere. DSC curves were obtained with a scan rate of 5 °C min^{-1} within the range −50 °C to +400 °C.

Thermogravimetric analysis (TGA)

Thermogravimetric analysis (TGA) was performed with a Mettler-Toledo STARe System TGA 2 equipped with a horizontal furnace LF (400 W, 1100 °C), balance XP5 (resolution 1 mg)

and cooling system HUBER Minichiller 600. TG curves were measured in an open ceramic crucible with a scan rate of 5 °C min^{-1} under an inert N_2 atmosphere within the range 25 °C to 400 °C.

TiO$_2$ nanotube layer fabrication

Self-organized TiO_2 nanotube layers (TNT layers) were fabricated *via* electrochemical anodization of Ti foils as described in our previous work.[52] The as-prepared amorphous 5 μm-thick TNT layers turned into the anatase phase after annealing in a muffle oven at 400 °C for 1 h.[53]

Atomic layer deposition of Ti$_x$P$_y$

The synthesis of Ti_xP_y thin films by thermal ALD (Beneq-TFS 200) was assessed within a temperature range from 150 to 250 °C with a base pressure of approximately 2 mbar using in-house synthesized TMS$_3$P and TMT$_3$P as the P precursors, and $TiCl_4$ (99.99+%, STREM) as a Ti precursor. The precursors TMS$_3$P and TMT$_3$P were heated up to increase the vapor pressure to 50 and 90 °C, respectively. N_2 (99.9999%) was used as a carrier gas applying a flow rate of 500 standard cubic centimeters per minute (sccm) in a continuous flow process. One ALD cycle was composed of the sequence: $TiCl_4$ pulse (500 ms)—N_2 purge (5 s)—P precursor pulse (1000 ms)—N_2 purge (10 s).

Post-annealing treatment

The as-deposited samples underwent a post-annealing treatment in the ALD chamber at 450 °C under vacuum (2 mbar) for 2 hours and 50 sccm of N_2 flow, applying 330 pulses of Ar (1.5 s) and 20 s of purging time. The heating rate applied was 2.6 °C min^{-1} and the samples were cooled down naturally.

Characterization techniques

The evaluation of the morphology and the thickness of the Ti_xP_y thin films on the different substrates was conducted using a field-emission scanning electron microscope (FE-SEM) JEOL JSM 7500F. SEM characterization was carried out applying an accelerating voltage of 5 kV, a beam current of 20 mA and a probe current of 30 pA. r-Filter was applied to combine signals (1 : 1) from secondary and backscattered electrons. The thickness of the Ti_xP_y thin films was measured and statistically evaluated using proprietary Nanomeasure software.

X-ray diffraction (XRD) analysis was performed using Panalytical Empyrean with a Cu tube and a Pixcel3D detector. Grazing incidence X-ray diffraction was performed to obtain the diffraction spectra of the as-deposited and post-annealed Ti_xP_y thin films. The incident angle was 1 degree. The patterns were recorded in the range of 5–65°, the step size was 0.026 degrees, and the time per step was 11 s.

X-Ray reflectivity (XRR) analysis was performed using on the incidence side a focusing mirror with a 1/32° divergence slit, a 1/16° antiscatter slit, a 0.04 rad Soller slit and a 4 mm mask. The sample was placed on the chi–phi-z cradle. On the diffraction side, a parallel plate collimator with a 0.18° slit was used together with a programmable attenuator and a Pixcel^{3D}

detector. X'pert reflectivity software was used to evaluate the data and run the fitting of the experimental data in order to estimate the thickness, density and roughness of the Ti_xP_y thin films.

The roughness and morphology of the Ti_xP_y thin films were determined by atomic force microscopy (AFM) in air using the NTEGRA (NT-MDT) system and applying tapping mode with a HA-HR tip (ScenSans) and a step of 8 nm. The roughness value was obtained as the mean value of 3 measurements of a scanned area of 1×1 μm^2.

X-ray photoelectron spectroscopy (XPS) (ESCA2SR, Scienta-Omicron) was employed to evaluate the chemical surface composition of Ti_xP_y thin films using a monochromatic AlKα (1486.7 eV) X-ray source operated at 200 W. The binding energy scale correction was carried out using the adventitious carbon C 1s at 284.8 eV. The survey and high-resolution (HR) spectra were recorded at a pass energy of 150 and 30 eV, respectively. Data analysis was performed with the CasaXPS program (Casasoftware Ltd). The Ti 2p spectra were fitted using a Shirley-type background with asymmetric Lorentzian function LA (1.2, 2.5, 120) for the Ti–P species and mixed Gaussian–Lorentzian functions GL (60) for the other Ti oxidation states. Also, the area ratio and the binding energy distance constraints between the spin–orbit splitting (Ti 2p$_{3/2}$ and Ti 2p$_{1/2}$), 2 : 1, and 6.0 eV (for Ti–P) and 5.7 eV (for other Ti oxidation states), respectively, were considered. The P 2p spectra were fitted using a Shirley-type background with asymmetric Lorentzian function LA (1.2, 2.5, 120) for the Ti–P and P–P species and mixed Gaussian–Lorentzian functions GL (30) for the P–O species. Also, the area ratio and the binding energy distance constraints between the spin–orbit splitting (P 2p$_{3/2}$ and P 2p$_{1/2}$), 2 : 1, and 0.84 eV, respectively, were considered. Last, but not least, it is worth noting that, to our knowledge, this is the first time that Ti_xP_y thin films have been fully characterized and analyzed (peak fitted) using XPS. Quantitative analysis was performed using the elemental sensitivity factors provided by the manufacturer.

The four-probe electrical characterization was performed on a custom-made box equipped with a head containing 4 probes arranged in line with 1 mm spacing in combination with a Keithley 4200A-SCS parameter analyzer. A standard method was employed when outer probes were determined for current bias, while the inner probes measured the voltage difference. The optimal measuring current of 30 mA was experimentally determined for all samples according to current sweeping in the range from 0 to 100 mA with a step of 5 mA. Five measurements were done on each sample at different places to obtain data for the calculation of the mean value and standard deviation.
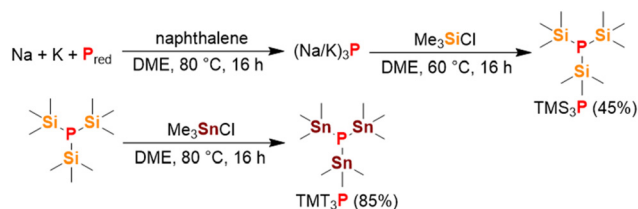
Results and discussion

TMT$_3$P was prepared by treating TMS$_3$P with Me$_3$SnCl according to a previously reported method[54,55] with some further modifications. In our case, the reaction was carried out in
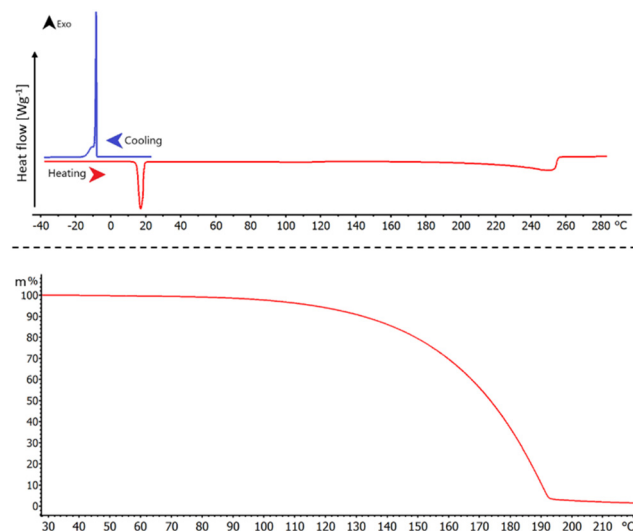
DME (1,2-dimethoxyethane), while the original syntheses used neat reactants; see the ESI† for further details. TMS$_3$P was prepared from (Na/K)$_3$P and Me$_3$SiCl in 45% yield.[56] Syntheses are shown in Scheme 1 with details including NMR and GC/MS characterization described in the ESI (see Fig. S1–S12†). TMT$_3$P is a colourless liquid well-soluble in a variety of organic solvents (*e.g.* hexane, toluene, benzene, THF, *etc.*). Unlike TMS$_3$P, TMT$_3$P is not pyrophoric when exposed to air, although careful treatment and precaution are recommended. Both TMS$_3$P and TMT$_3$P are air-sensitive substances and, therefore, must be stored under an inert atmosphere in a dry and cool place. When properly stored, the chemical stability lasts for several months. However, exposing C$_6$D$_6$ solution of TMT$_3$P to air for a few days resulted in a mixture of TMT$_x$PH$_y$ and PH$_3$, as observed from the ^{31}P-NMR spectrum. However, the decomposition pathway was not investigated in detail.

The boiling point of TMT$_3$P at 0.5 torr is 120 °C as determined by distillation, while DSC estimates 250 °C at the atmospheric pressure (Fig. 1). The boiling is not accompanied by any decomposition process and no visible residue is left in the measuring crucible, which was further confirmed by TG analysis revealing smooth and gradual evaporation with zero residue. The synthesis of Ti$_x$P$_y$ thin films by thermal ALD (described in detail in the Experimental section) was explored within a temperature range from 150 to 250 °C using both
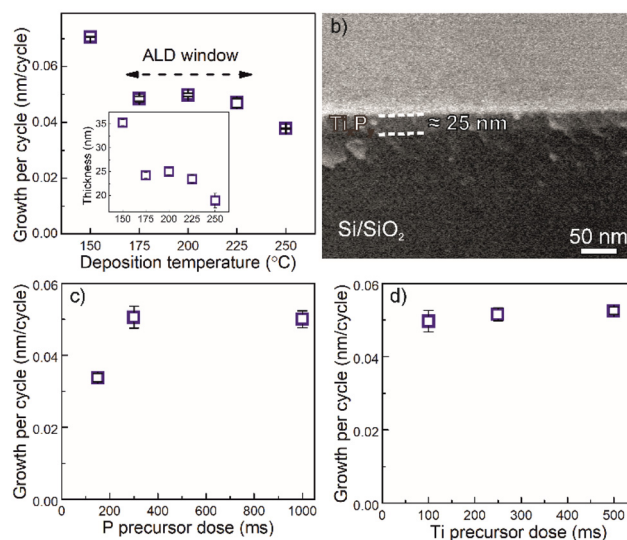
TMS$_3$P and TMT$_3$P as the P-precursors, and TiCl$_4$ as a Ti precursor. In order to determine the ALD window and the effect of the deposition temperature on the Ti$_x$P$_y$ growth rate, ALD processes were conducted applying 500 ALD cycles at different deposition temperatures: 150, 175, 200, 225 and 250 °C. The effect of the substrates on the ALD growth of Ti$_x$P$_y$ thin films was addressed by the use of substrates of different nature such as Si/SiO$_2$ wafers, soda lime glass and 5 μm-thick TiO$_2$ nanotube (TNT) layers. Using TMS$_3$P as the P-precursor, the ALD processes at 150 and 250 °C did not yield any deposition. An additional ALD process carried out at 300 °C to rule out the reaction between precursors was thermally limited in the range of deposition temperatures explored. The result at 300 °C was identical, *i.e.*, no deposition was found. In contrast, when using TMT$_3$P as the P precursor the deposition of silver-colored films was observed. Thus, the results obtained using TMT$_3$P as the P precursor evaluating the growth rate as a function of the deposition temperature are shown in Fig. 2a. Therein, an ALD window was identified in a temperature range between 150 °C and 225 °C with a GPC value of ≈0.05 nm per cycle applying TMT$_3$P and TiCl$_4$ doses of 1000 and 500 ms, respectively. The thicknesses of the Ti$_x$P$_y$ films deposited were measured from cross-sectional scanning electron microscopy (SEM) images of the Si/SiO$_2$ substrates (see Fig. 2b and Fig. S13†). Importantly, the self-saturated nature of the ALD process was assessed by varying one precursor pulse length, while keeping the rest of the parameters of the process fixed.

Scheme 1 The reaction pathway towards TMS$_3$P and TMT$_3$P.

Fig. 1 DSC curve (top) and TG record (bottom) of TMT$_3$P.

Fig. 2 (a) Thickness dependence of the Ti$_x$P$_y$ thin on the deposition temperature after 500 ALD cycles on Si/SiO$_2$ wafer using TMT$_3$P as the P precursor. ALD window was identified between 175 and 225 °C. (b) Representative cross-sectional SEM image of a Ti$_x$P$_y$ thin film with a thickness of ≈25 nm on a Si/SiO$_2$ wafer after 500 cycles at a temperature of 200 °C, where the Ti$_x$P$_y$ film is indicated by dashed lines. Ti$_x$P$_y$ growth rate on Si/SiO$_2$ wafers at 200 °C after applying 500 ALD cycles as a function of (c) the TMT$_3$P precursor dose and (d) TiCl$_4$ dose (each inset showing the corresponding thickness). Saturation regime was observed for all the TiCl$_4$ dose values and for P precursor dose value above 150 ms.

Thus, a set of ALD processes was performed at 200 °C applying 500 ALD cycles on Si/SiO$_2$ wafers. The doses applied for the P precursor were 150, 300 and 1000 ms (keeping the TiCl$_4$ dose constant at 500 ms), while the doses for TiCl$_4$ were 100, 250 and 500 ms (keeping the P precursor TMT$_3$P constant at 1000 ms). The thickness of the resulting Ti$_x$P$_y$ thin films measured from cross-sectional SEM images (see Fig. S14†) and the corresponding GPC shown in Fig. 2c and d verified that the reaction between TMT$_3$P and TiCl$_4$ follows the ALD principle for all the TiCl$_4$ pulse durations and for a TMT$_3$P pulse duration ≥150 ms, exhibiting a growth rate value of ≈0.05 nm per cycle. To further confirm the ALD nature of the reaction, ALD processes applying different numbers of cycles, namely, 250, 375, 500, 750 and 1000, were performed using Si/SiO$_2$ wafers and TNT layers. Cross-sectional SEM images allowed us to determine the thicknesses of the Ti$_x$P$_y$ thin films on Si/SiO$_2$ wafers and TNT layers (see Fig. S15†). The plot of the thin film thickness as a function of the number of ALD cycles shown in Fig. S16† verified the ALD nature of the reaction (i.e. the linear relationship between the thickness and the number of ALD cycles) on both Si/SiO$_2$ wafers and TNT layers with an estimated GPC of 0.051 nm per cycle and 0.043 nm per cycle, respectively. A nucleation delay, estimated from the fitting line, was observed for the Si/SiO$_2$ wafers (≈20 ALD cycles) and the TNT layers (≈50 ALD cycles). The nucleation delay is discussed ahead in detail. X-Ray reflectivity (XRR) measurements were performed (see the Experimental section for details) to provide complementary information on the thin film thickness measurements and estimate the density and roughness of the Ti$_x$P$_y$ thin films deposited on Si/SiO$_2$ wafers as shown in Fig. S17.† The estimated thin film thicknesses were in good agreement with those obtained from cross-sectional SEM images (see Table S1†). The density of the Ti$_x$P$_y$ thin films was within the nominal value range (≈3.95–4.1 g cm^{-3}) for the thickest films, while it was slightly lower for the thinner ones (3.5–3.6 g cm^{-3}). Regarding the surface roughness, it increased along with the thickness of the thin film.
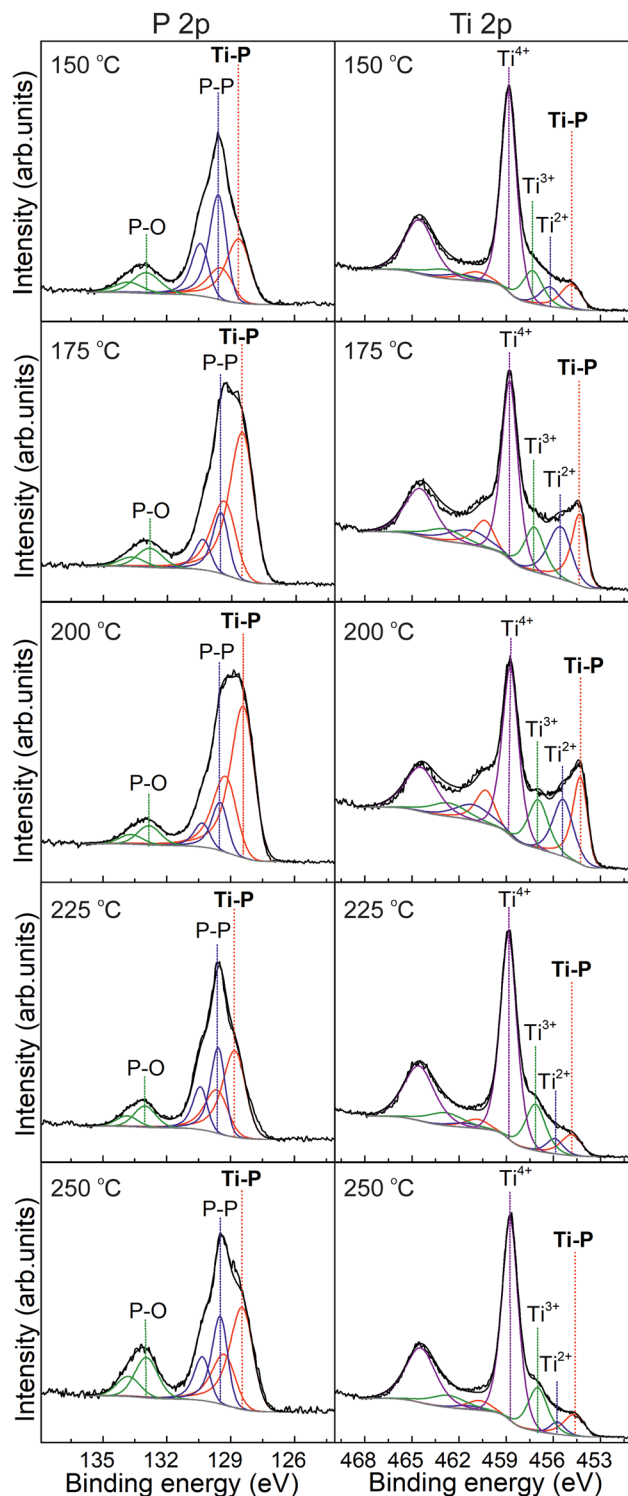
X-ray diffraction (XRD) analyses of the as-deposited Ti$_x$P$_y$ thin films on Si/SiO$_2$ wafers showed no apparent crystalline nature (see Fig. S18†) even at the highest deposition temperature, i.e., 250 °C. Nevertheless, crystalline titanium phosphide films were prepared by a post-annealing process carried out using Si/SiO$_2$ wafers coated with 250 and 500 ALD cycles at 450 °C for 2 h (see details in the Experimental section). The XRD pattern shown in Fig. S18† exhibited a set of diffraction peaks indicating a hexagonal structure.[57] The diffraction peaks and the corresponding lattice planes observed were 29.5° (010), 30.5° (011), 33.4° (012), 37.7° (013), 43.1° (014), 49.3° (015) and 52.4° (110). Additional peaks denoted with a diamond and an asterisk corresponded to metallic tin (originating from incomplete ligand exchange reaction as described ahead) and the substrate, respectively. XRR measurements were performed to evaluate the potential impact of the post-annealing process on the density of the Ti$_x$P$_y$ thin films. The results revealed, as compared to those obtained from the as-deposited samples, a slight increase of the density values,

3.87 g cm^{-3} and 4.0 g cm^{-3}, for the samples coated with 250 and 500 ALD cycles, respectively.

The morphology and roughness of the as-deposited Ti$_x$P$_y$ were characterized by scanning electron microscopy (SEM) and atomic force microscopy (AFM). Fig. S19† shows the SEM surface topography of the Ti$_x$P$_y$ thin film deposited on a Si/SiO$_2$ wafer with a well-defined granular shape. Fig. S20a–e† show the AFM images of Ti$_x$P$_y$ thin films deposited after 500 ALD cycles on Si/SiO$_2$ wafers at different temperatures. The results showed how higher deposition temperatures induced an increase of the Ti$_x$P$_y$ thin film roughness, as indicated by the root-mean-square roughness values (R_q; see Fig. S20f†).

The surface chemical composition of the Ti$_x$P$_y$ thin films was extensively characterized by X-ray photoelectron spectroscopy (XPS) as a function of different ALD parameters such as deposition temperature, dosing time of TMT$_3$P and TiCl$_4$, and the type of substrate. Fig. S21† shows the XPS survey spectra of Ti$_x$P$_y$ obtained after 500 ALD cycles on Si/SiO$_2$ wafers at different deposition temperatures (150, 175, 200, 225 and 250 °C) revealing the presence of Ti, P, C, O, and traces of Cl and Sn. The presence of a residual content of Cl and Sn indicates that the ligand exchange reaction between both P and Ti precursors is not always complete. The elemental composition of the Ti$_x$P$_y$ deposited at different temperatures obtained from XPS analysis is shown in Table S2.† Regarding the O content, the samples were exposed to O-free precursors so that the content of O could be ascribed to the oxidation due to exposure to air before XPS analysis. The deconvoluted HR P 2p and Ti 2p XPS spectra obtained from the Ti$_x$P$_y$ thin films deposited at different temperatures on Si/SiO$_2$ wafers after 500 ALD cycles shown in Fig. 3 demonstrated the deposition of Ti$_x$P$_y$. The peak fitting of the HR Ti 2p XPS spectra with its characteristic spin–orbit splitting of Ti 2p$_{3/2}$ and Ti 2p$_{1/2}$ revealed the presence of different species of Ti. Thus, the content of Ti$_x$P$_y$ was verified by the peaks at ≈454.2 and ≈460.2 eV. In addition, the coexistence of Ti$_x$P$_y$ with different oxidation states of Ti, namely Ti^{2+}, Ti^{3+} and Ti^{4+}, was indicated by the peaks at ≈455.4 and ≈461.1 eV (Ti^{2+}), ≈457.0 and ≈462.7 eV (Ti^{3+}), and ≈458.7 and ≈464.4 eV (Ti^{4+}). The presence of Ti^{4+} was related to the minor content of titanium phosphate and unreacted Ti precursor, while the action of TMT$_3$P as a reducing agent (due to the content of P^{3-}) over Ti^{4+} would be behind the presence of Ti^{2+} and Ti^{3+}. Regarding the peak fitting of the HR P 2p XPS spectra with its characteristic spin–orbit splitting of P 2p$_{3/2}$ and P 2p$_{1/2}$, it allowed the identification of the presence of 3 different species of P. The peaks at ≈128.9 and ≈129.1 eV verified the presence of titanium phosphide (Ti–P), while the peaks at ≈129.4 and ≈130.3 eV accounted for elemental P (P–P). The latter suggested the ALD growth of P-rich Ti$_x$P$_y$ with the existence of extensive P–P bonding motifs where the Ti cation(s) are embedded. The minor content of titanium phosphate (P–O) was confirmed by the peaks at ≈132.8 and ≈133.6 eV. Thus, XPS results showed the presence of Ti$_x$P$_y$ along with other Ti and P species. The atomic concentration of the different P species is shown in Table 1. It suggests the coexistence of the ligand exchange

Fig. 3 High-resolution XPS spectra of P 2p and Ti 2p obtained from Ti_xP_y thin films after 500 ALD cycles at different deposition temperatures.

Table 1 Atomic concentration of the different P-based species from the HR deconvoluted P 2p XPS spectral peak obtained from Ti_xP_y thin films deposited on Si/SiO_2 wafers after 500 ALD cycles at different temperatures using a TMT_3P dose of 1000 ms and a $TiCl_4$ dose of 500 ms

Deposition temperature (°C)	P atomic concentration [%]		
	Phosphide (P^-)	Elemental phosphorus (P–P)	Phosphate (P–O)
150	40.37	46.43	13.20
175	72.01	19.23	8.76
200	75.50	16.04	8.46
225	54.40	34.27	11.33
250	51.61	30.10	18.29

the deposition temperatures 175 and 200 °C as the optimal ones, allowing us to attain thin films with the lowest/highest content of titanium phosphate/Ti_xP_y, respectively. In fact, the Ti_xP_y thin films deposited at those temperatures have lower values of the Ti/P ratio indicating P-enriched thin films (see Table S2†). These results demonstrated the effect of the deposition temperature on the chemical composition of the Ti_xP_y thin films. Thus, at a low deposition temperature (150 °C) the reaction can be thermally limited, while a deposition temperature of 250 °C could induce a partial decomposition of the P precursor and/or desorption of the material.

XPS also characterized the effects of different doses of both precursors (TMT_3P and $TiCl_4$) during the ALD process on the chemical composition of the Ti_xP_y thin films on Si/SiO_2 wafers as shown in Fig. S22 and S23.† The XPS analysis was carried out characterizing Ti_xP_y thin films deposited after 500 ALD cycles at 200 °C and whose elemental composition, shown in Table S3,† indicated that the effects of different doses of both precursors on the chemical composition were not significant. Thus, similar contents of the different elements as well as slight differences of the Ti/P ratios were observed. Likewise, the contents of the different P and Ti species evaluated by the peak fitted HR P 2p and Ti 2p XPS spectra did not differ substantially showing principally a content of phosphide and Ti exhibiting different oxidation states (see Tables S4 and S5,† respectively). These results indicated that the different doses of both precursors used, TMT_3P and $TiCl_4$, did not have any significant impact on the chemical composition of the Ti_xP_y thin films deposited. Similarly, the effect of the substrate on the chemical composition was evaluated by XPS using Ti_xP_y thin films deposited after 500 ALD cycles at 200 °C applying a 1000 ms dose of TMT_3P and a 500 ms dose of $TiCl_4$ (see Fig. S24†). The substrates studied were Si/SiO_2 wafers, soda lime glass and TNT layers. Although the elemental composition shown in Table S6† was found to be similar in all the cases, the atomic concentrations of the different P species revealed a significant finding. As compared to the Ti_xP_y thin films deposited on soda lime glass and Si/SiO_2 wafers, those films deposited on TNT layers (see Table S7†) contained higher atomic percentage phosphate and elemental P (at the expense of the content of phosphide), and Ti^{4+} (see Table S8†).

reactions to form Ti_xP_y, along with redox reactions that occur concurrently. The redox reaction mechanism leading to the formation of elemental P and a wide variety of Ti oxidation states is described in detail later. The obtained results indicate

Initially, this outcome could be ascribed to either a dependence of the chemical composition of the Ti_xP_y thin films on the type of substrate or to a thinner Ti_xP_y thin film deposited on TNT layers (due to the lower growth mentioned earlier on such a substrate). In order to determine the origin of this result, TNT layers coated at 200 °C with different numbers of Ti_xP_y ALD cycles, namely 25, 125, 250 and 500, were characterized by XPS (see Fig. 4). The results indicated that the content of T^{4+} exhibited a constantly dropping value (see Table S9†), and the content of phosphate also decreased after 250 ALD cycles (see Table S10†) down to a certain value ($\approx$20%). Yet it did not further decrease for a growing number of ALD cycles (500 cycles). This suggested a dependence of the chemical composition of the Ti_xP_y thin films on the type of substrate as

Si/SiO_2 wafer and soda lime glass exhibited a lower content of phosphate at around 10%.

Here, it is worthy to note that the XPS results obtained from the initial stage of the ALD process provided unique information to gain a deeper insight into the origin of the nucleation delay, the evolution of the chemical composition of the surface and the growing process of the Ti_xP_y thin films, as demonstrated in previous works.[58,59] Peak fitted HR P 2p and Ti 2p XPS spectra shown in Fig. 4 illustrated how at an early stage of the ALD process (25 cycles) the dominant reactions at the interface with the substrate are the formation of phosphate (peaks at $\approx$133.0 and $\approx$133.8 eV) and titanium oxide (peaks at $\approx$458.8 and $\approx$464.5 eV). The main feature observed in the evolution of the chemical composition after 125 ALD cycles was the emergence of elemental P as indicated by the XPS peaks observed in the fitted HR P 2p XPS spectrum at $\approx$129.5 and $\approx$130.4 eV. Concurrently, the Ti 2p XPS spectrum revealed the presence of reduced species of Ti, i.e., Ti^{3+} and Ti^{2+}. Significantly, the growth of Ti_xP_y was observed only after 250 ALD cycles as indicated by both the peak fitted HR Ti 2p XPS spectra exhibiting peaks at $\approx$454.2 and $\approx$460.2 eV, and the peak fitted HR P 2p XPS spectra at $\approx$128.4 and $\approx$129.2 eV. Interestingly, the results also revealed the coexistence of a higher content of reduced species of Ti (Ti^{3+} and Ti^{2+}) and elemental P as compared to that with 125 ALD cycles. At the same time, with an increasing number of ALD cycles (250 and 500) a strong intensity fading of the phosphate peaks was observed, indicating that the formation of P–O species was mainly constrained to the substrate interface. In the case of the presence of P–O species also observed for a higher number of cycles, it was ascribed as mentioned above to oxidation processes due to exposure of the samples to air before XPS analysis, and/or residual H_2O or O_2 content in the ALD reactor during the ALD process.

Based on these XPS results, a tentative description of the origin of the nucleation delay as well as the conditions needed for the growth of Ti_xP_y is provided as follows. Considering that the oxidation states of P and Ti in Ti_xP_y are P^{-3} and Ti^{3+}, it means that the Ti^{4+} from the Ti precursor ($TiCl_4$) must be reduced to Ti^{3+}. The only reducing agent involved in the ALD reactions is TMT_3P which oxidized to P^0 at the expense of forming reduced Ti species. This redox reaction describes the formation of the elemental P and the reduced Ti species, Ti^{3+} and Ti^{2+}. This implies that during the early stage of the ALD process no Ti_xP_y grows, but the elemental P and reduced species of Ti are formed as indicated by XPS results shown in Fig. 4 and Tables S9 and S10.† However, after certain numbers of ALD cycles, the elemental P loading is high enough to start acting as a reducing agent allowing the P precursor to react with the reduced Ti species and trigger the growth of Ti_xP_y as observed in this work after 250 ALD cycles. Thus, the elemental P can act as a "seeding" layer prompting the growth of Ti_xP_y by playing a dual role: (i) avoiding the oxidation of P^{3-} from TMT_3P and (ii) promoting the reduction of Ti^{4+} to Ti^{3+}. Therefore, the nucleation delay would be related to the number of ALD cycles required to reach the critical elemental P loading that enables the growth of Ti_xP_y. Scheme 2 illustrates
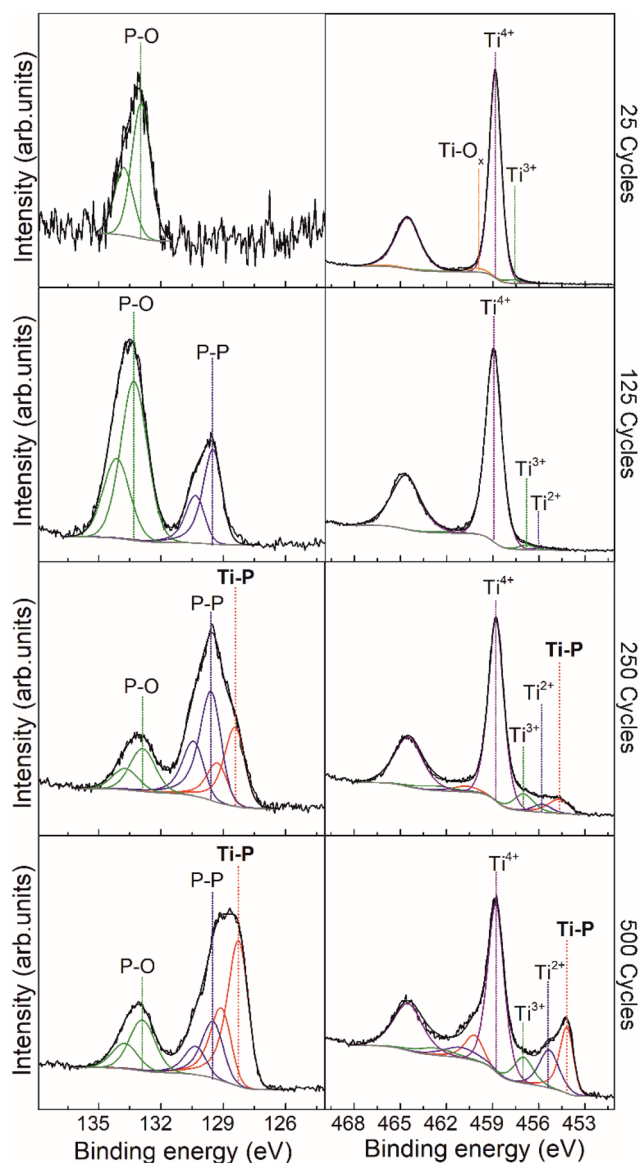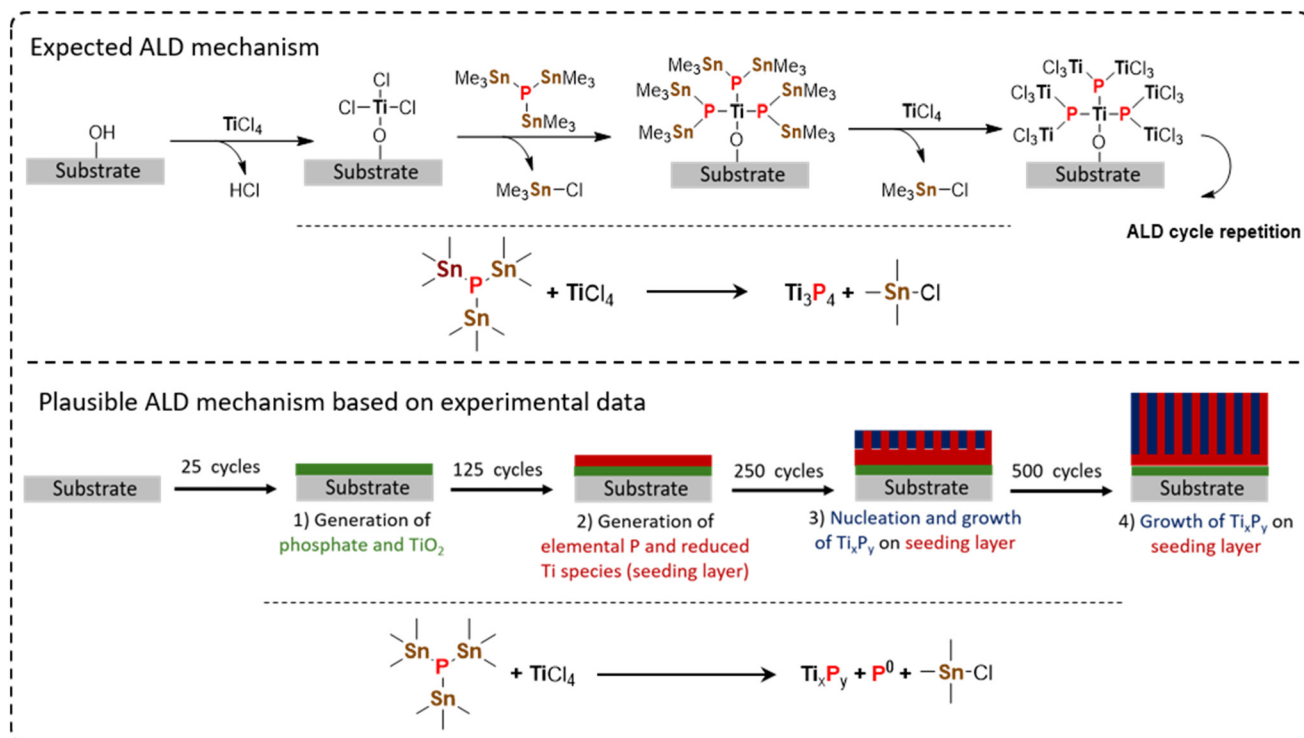

Fig. 4 Peak fitted high-resolution XPS of Ti 2p (left) and P 2p (right) from Ti_xP_y thin films at 200 °C obtained after different number of ALD cycles (25, 125, 250 and 500) on TNT layers.

Scheme 2 (Top) Illustrative description of the expected ALD mechanism for the growth of Ti_xP_y. (Bottom) Plausible ALD mechanism proposed to describe the growth of Ti_xP_y based on experimental data.

the initially expected ALD mechanism and the tentative description of the growth of Ti_xP_y based on the experimental data as described above.

Regarding the electrical resistance of the P-rich Ti_xP_y thin films, it was evaluated by 4-probe measurements as described in the Experimental section, using the Ti_xP_y thin films deposited on soda lime glass after 500 ALD cycles at different temperatures, that is electrical resistance was of the order of hundreds of Ohms (Fig. S25†) which was in line with previous works reporting the electrical resistance of diverse P-rich metal phosphides. For instance, relatively low electrical resistance values in the range of 10–300 Ω were reported for FeP_2, CoP_3 and NiP_2 pellet samples.[60] The limited electrical conductivity of P-rich metal phosphides accounted for the decrease in metal–metal bonds making most P-rich phosphides semiconductors.[61]

Conclusions

Overall, herein the synthesis of titanium phosphide (Ti_xP_y) by thermal ALD is demonstrated for the first time using a new in-house P precursor – Tris(trimethyltin)phosphide (TMT_3P) – combined with $TiCl_4$. The chemical reaction proved to follow the ALD principle and exhibited an ALD window between 175 °C and 225 °C. The as-deposited Ti_xP_y thin films were characterized by different techniques showing a granular surface and electrical resistance of the order of hundreds of Ohms. Post-annealing treatment produced crystalline Ti_xP_y films exhibiting a hexagonal structure. Extensive XPS analyses were carried out to assess the

effect on the chemical composition with different ALD parameters such as deposition temperature, dosing time of TMT_3P and $TiCl_4$, and the type of substrate. The results revealed the deposition of P-rich titanium phosphide with a chemical composition dependence on the deposition temperature and the type of substrate. Based on XPS results, a tentative description of the Ti_xP_y growth as a function of the number of ALD cycles was provided. This work opens new paths through novel in-house P precursors to the synthesis of metal phosphides by ALD and all the benefits this technique provides.

Author contributions

R. Zazpe, J. Charvot, F. Bureš and J. M. Macak conceived the idea, designed the experiments and supervised the research. R. Zazpe, J. Charvot, and J. Rodriguez-Pereira conducted the experiments. J. Charvot and H. Sopha synthesized the precursors and materials. J. Rodriguez-Pereira, L. Hromádko, M. Kurka and K. Baishya performed materials characterization. R. Zazpe drafted the manuscript through the contributions of all authors, and all the authors revised and gave approval to the final version of the manuscript.

Data availability

The data supporting this article have been included as part of the ESI.†

Conflicts of interest

There are no conflicts to declare.

Acknowledgements

References

1 S. H. Li, M. Y. Qi, Z. R. Tang and Y. J. Xu, *Chem. Soc. Rev.*, 2021, **50**, 7539–7586.

2 Y. Shi, M. Li, Y. Yu and B. Zhang, *Energy Environ. Sci.*, 2020, **13**, 4564–4582.

3 H. Zhao and Z.-Y. Yuan, *Catal. Sci. Technol.*, 2017, **7**, 330–347.

4 G. Li, Y. Feng, Y. Yang, X. Wu, X. Song and L. Tan, *Nano Mater. Sci.*, 2024, **6**, 174–192.

5 A. Agarwal and B. R. Sankapal, *J. Mater. Chem. A*, 2021, **9**, 20241–20276.

6 P. Wei, W. Han, L. Xie, L. Zhu, B. He and X. Cao, *Trends Food Sci. Technol.*, 2024, **151**, 104611.

7 X. Lu, K. Yan, Z. Yu, J. Wang, R. Liu, R. Zhang, Y. Qiao and J. Xiong, *ChemSusChem*, 2024, **17**, e202301687.

8 P. Xiao, W. Chen and X. Wang, *Adv. Energy Mater.*, 2015, **5**, 1500985.

9 W. Wu, S. Luo, Y. Huang, H. He, P. K. Shen and J. Zhu, *Mater. Chem. Front.*, 2024, **8**, 1064–1083.

10 K. Bhunia, M. Chandra, S. Kumar Sharma, D. Pradhan and S.-J. Kim, *Coord. Chem. Rev.*, 2023, **478**, 214956.

11 M. U. Shahid, T. Najam, M. H. Helal, I. Hossain, S. M. El-Bahy, Z. M. El-Bahy, A. ur Rehman, S. S. A. Shah and M. A. Nazir, *Int. J. Hydrogen Energy*, 2024, **62**, 1113–1138.

12 L. Hong, R. Guo, Y. Yuan, X. Ji, Z. Lin, Z. Li and W. Pan, *ChemSusChem*, 2021, **14**, 539–557.

13 R. W. Johnson, A. Hultqvist and S. F. Bent, *Mater. Today*, 2014, **17**, 236–246.

14 N. Pinna and M. Knez, *Atomic Layer Deposition of Nanostructured Materials*, Wiley-VCH Verlag GmbH & Co. KGaA, Weinheim, Germany, 2012.

15 N. E. Richey, C. de Paula and S. F. Bent, *J. Chem. Phys.*, 2020, **152**, 040902.

16 K. J. Hughes and J. R. Engstrom, *J. Vac. Sci. Technol., A*, 2012, **30**, 01A102.

17 S. Kim, S. Lee, S. Y. Ham, D. H. Ko, S. Shin, Z. Jin and Y. S. Min, *Appl. Surf. Sci.*, 2019, **469**, 804–810.

18 J. W. Maina, A. Merenda, M. Weber, J. M. Pringle, M. Bechelany, L. Hyde and L. F. Dumée, *Crit. Rev. Solid State Mater. Sci.*, 2021, **46**, 468–489.

19 M. Tiitta, E. Nykänen, P. Soininen, L. Niinistö, M. Leskelä and R. Lappalainen, *Mater. Res. Bull.*, 1998, **33**, 1315–1323.

20 H. Yuan, B. Luo, S. A. Campbell and W. L. Gladfelter, *Electrochem. Solid-State Lett.*, 2011, **14**, H181.

21 L. Henderick, A. Dhara, A. Werbrouck, J. Dendooven and C. Detavernier, *Appl. Phys. Rev.*, 2022, **9**, 011310.

22 M. Nieminen, L. Niinistö and R. Lappalainen, *Mikrochim. Acta*, 1995, **119**, 13–22.

23 J. Hämäläinen, J. Holopainen, F. Munnik, M. Heikkilä, M. Ritala and M. Leskelä, *J. Phys. Chem. C*, 2012, **116**, 5920–5925.

24 M. K. Wiedmann, D. H. K. Jackson, Y. J. Pagan-Torres, E. Cho, J. A. Dumesic and T. F. Kuech, *J. Vac. Sci. Technol., A*, 2012, **30**, 01A134.

25 K. B. Gandrud, A. Pettersen, O. Nilsen and H. Fjellvåg, *J. Mater. Chem. A*, 2013, **1**, 9054–9059.

26 T. Dobbelaere, A. K. Roy, P. Vereecken and C. Detavernier, *Chem. Mater.*, 2014, **26**, 6863–6871.

27 T. Dobbelaere, M. Minjauw, T. Ahmad, P. M. Vereecken and C. Detavernier, *J. Non-Cryst. Solids*, 2016, **444**, 43–48.

28 T. Dobbelaere, F. Mattelaer, J. Dendooven, P. Vereecken and C. Detavernier, *Chem. Mater.*, 2016, **28**, 3435–3445.

29 T. Dobbelaere, F. Mattelaer, A. K. Roy, P. Vereecken and C. Detavernier, *J. Mater. Chem. A*, 2017, **5**, 330–338.

30 T. Dobbelaere, F. Mattelaer, P. M. Vereecken and C. Detavernier, *J. Vac. Sci. Technol., A*, 2017, **35**, 041513.

31 L. Henderick, R. Blomme, M. Minjauw, J. Keukelier, J. Meersschaut, J. Dendooven, P. Vereecken and C. Detavernier, *Dalton Trans.*, 2022, **51**, 2059–2067.

32 M. Nisula, Y. Shindo, H. Koga and M. Karppinen, *Chem. Mater.*, 2015, **27**, 6987–6993.

33 R. B. Nuwayhid, A. Jarry, G. W. Rubloff and K. E. Gregorczyk, *ACS Appl. Mater. Interfaces*, 2020, **12**, 21641–21650.

34 J. Su, T. Tsuruoka, T. Tsujita, Y. Nishitani, K. Nakura and K. Terabe, *Chem. Mater.*, 2019, **31**, 5566–5575.

35 L. Henderick, H. Hamed, F. Mattelaer, M. Minjauw, M. Nisula, J. Meersschaut, J. Dendooven, M. Safari, P. Vereecken and C. Detavernier, *J. Power Sources*, 2021, **497**, 229866.

36 H. Zhang, D. J. Hagen, X. Li, A. Graff, F. Heyroth, B. Fuhrmann, I. Kostanovskiy, S. L. Schweizer, F. Caddeo, A. W. Maijenburg, S. Parkin and R. B. Wehrspohn, *Angew. Chem., Int. Ed.*, 2020, **59**, 17172–17176.

37 A. V. Uvarov, A. S. Gudovskikh, V. N. Nevedomskiy, A. I. Baranov, D. A. Kudryashov, I. A. Morozov and J.-P. Kleider, *J. Phys. D: Appl. Phys.*, 2020, **53**, 345105.

38 N. Otsuka, J. I. Nishizawa, H. Kikuchi and Y. Oyama, *Jpn. J. Appl. Phys.*, 1999, **38**, L20–L23.

39 E. Graugnard, V. Chawla, D. Lorang and C. J. Summers, *Appl. Phys. Lett.*, 2006, **89**, 211102.

40 M. Fujii, H. Iwanaga and S. Motojima, *J. Cryst. Growth*, 1996, **166**, 99–103.

41 S. Motojima, K. Haguri, Y. Takahashi and K. Sugiyama, *J. Less-Common Met.*, 1979, **64**, 101–106.

42 C. S. Blackman, C. J. Carmalt, S. A. O'Neill, I. P. Parkin, L. Apostolico and K. C. Molloy, *Chem. Mater.*, 2004, **16**, 1120–1125.

43 T. Sarnet, T. Hatanpää, M. Laitinen, T. Sajavaara, K. Mizohata, M. Ritala and M. Leskelä, *J. Mater. Chem. C*, 2016, **4**, 449.

44 V. Pore, K. Knapas, T. Hatanpää, T. Sarnet, M. Kemell, M. Ritala, M. Leskelä and K. Mizohata, *Chem. Mater.*, 2011, **23**, 247–254.

45 S. He, A. Bahrami, X. Zhang, J. Julin, M. Laitinen and K. Nielsch, *Mater. Today Chem.*, 2023, **32**, 101650.

46 M. Al Hareri and D. J. H. Emslie, *Chem. Mater.*, 2022, **34**, 2400–2409.

47 Y. Kim, B. Han, Y. J. Kim, J. Shin, S. Kim, R. Hidayat, J. M. Park, W. Koh and W. J. Lee, *RSC Adv.*, 2019, **9**, 17291.

48 E. Atosuo, P. Deminskyi, K. Mizohata, T. Hatanpää and M. Ritala, in *ALD/ALE 2024, Helsinki; ALD_of_Co2P _Thin Films, Conference presentation*, AVS, Helsinki, 2024, p. 47.

49 E. W. Abel, D. A. Armitage and D. B. Brady, *Trans. Faraday Soc.*, 1966, **62**, 3459.

50 Q. M. Cheng, O. Stark, F. Stowasser, A. Wohlfart and R. A. Fischer, *J. Mater. Chem.*, 2002, **12**, 2470–2474.

51 P. S. Schofield, *The synthesis of indium nitride quantum dots*, University of St Andrews, 2003.

52 S. Das, H. Sopha, M. Krbal, R. Zazpe, V. Podzemna, J. Prikryl and J. M. Macak, *ChemElectroChem*, 2017, **4**, 495–499.

53 M. Motola, L. Hromadko, J. Prikryl, H. Sopha, M. Krbal and J. M. Macak, *Electrochim. Acta*, 2020, **352**, 136479.

54 H. Schumann and L. Rösch, *Chem. Ber.*, 1974, **107**, 854–868.

55 D. K. Harris and M. G. Bawendi, *J. Am. Chem. Soc.*, 2012, **134**, 20211–20213.

56 M. Z. Bani-Fwaz, A. E. Fazary and G. Becker, *J. Organomet. Chem.*, 2017, **846**, 51–65.

57 C. Blackman, C. J. Carmalt, I. P. Parkin, S. O'Neill, L. Apostolico, K. C. Molloy and S. Rushworth, *Chem. Mater.*, 2002, **14**, 3167–3173.

58 R. Zazpe, R. Krumpolec, H. Sopha, J. Rodriguez-Pereira, J. Charvot, L. Hromádko, E. Kolíbalová, J. Michalička, D. Pavliňák, M. Motola, J. Příkryl, M. Krbal, F. Bureš and J. M. MacAk, *ACS Appl. Nano Mater.*, 2020, **3**, 12034–12045.

59 R. Zazpe, H. Sopha, J. Charvot, R. Krumpolec, J. Rodriguez-Pereira, J. Michalička, J. Mistrík, D. Bača, M. Motola, F. Bureš and J. M. Macak, *Appl. Mater. Today*, 2021, **23**, 101017.

60 N. Coleman, M. D. Lovander, J. Leddy and E. G. Gillan, *Inorg. Chem.*, 2019, **58**, 5013–5024.

61 Y. Ma, M. A. Ud Din, W. Guo, Q. Wu and N. Cheng, *Mater. Sci. Semicond. Process.*, 2023, **167**, 107812.